The influence of sea- and land-breeze circulations on the diurnal variability of precipitation over a tropical island

Lei Zhu[1,2,3], Zhiyong Meng[1*], Fuqing Zhang[2,3], Paul M. Markowski[2]

[1]*Laboratory for Climate and Ocean-Atmosphere Studies, Department of Atmospheric and Oceanic Sciences, School of Physics, Peking University, Beijing, China*

[2]*Department of Meteorology and Atmospheric Science, The Pennsylvania State University, University Park, Pennsylvania*

[3] *Center for Advanced Data Assimilation and Predictability Techniques, The Pennsylvania State University, University Park, Pennsylvania*

[*]*Corresponding author address:* Dr. Zhiyong Meng, Laboratory for Climate and Ocean–Atmosphere Studies, Department of Atmospheric and Oceanic Sciences, School of Physics, Peking University, Beijing, China.

E-mail: zymeng@pku.edu.cn

Abstract

This study examines the diurnal variation of precipitation over Hainan Island in the South China Sea using gauge observations from 1950 to 2010 and CMORPH satellite estimates from 2006 to 2015, as well as numerical simulations. The simulations are the first to use climatological mean initial and lateral boundary conditions to study the dynamic and thermodynamic processes (and the impacts of land-sea breeze circulations) that control the rainfall distribution and climatology. Precipitation is most significant from April to October, and exhibits a strong diurnal cycle resulting from land/sea breeze circulations. More than 60% of the total annual precipitation over the island is attributable to the diurnal cycle with a significant monthly variability. The CMORPH and gauge datasets agree well, except that the CMORPH data underestimates precipitation and has a 1-h delay of peaks. The diurnal cycle of the rainfall and the related land/sea breeze circulations during May and June were well captured by convection-permitting numerical simulations with WRF, which were initiated from 10-year average ERA-interim reanalysis. The simulations have a slight overestimation of rainfall amounts and a 1-h delay in peak rainfall time. The diurnal cycle of precipitation is driven by the occurrence of moist convection around noontime owing to low-level convergence associated with the sea breeze circulations. The precipitation intensifies rapidly thereafter and peaks in the afternoon with the collisions of sea breeze fronts from different sides of the island. Cold pools of the convective storms contribute to the inland propagation of the sea breeze. Generally, precipitation dissipates quickly in the evening due to the cooling and stabilization of the lower troposphere and decrease of boundary-layer moisture. Interestingly, the rather high island orography is not a dominant factor in the diurnal variation of the precipitation over the island.

1. Introduction

On tropical islands, the diurnal precipitation cycle tends to be driven by the land-sea breeze (LSB), as well as mountain-valley wind systems (Mapes et al. 2003; Qian 2008; Crosman and Horel 2010). Both rain gauge and satellite observations indicate that rainfall peaks in the late afternoon over inland regions, and in the early morning or evening offshore (Yang and Slingo 2001).

The emergence of high temporal and spatial resolution satellite-estimated precipitation observations, such as those provided by Tropical Rainfall Measuring Mission (TRMM, Huffman et al. 2007) and Climate Prediction Center Morphing Technique **(**CMORPH, Joyce et al. 2004), has greatly improved our understanding of tropical precipitation. Precipitation amounts are much higher over tropical islands than their surrounding oceans (Qian 2008). More than 34% of the total precipitation in the tropics is attributable to precipitation over land (Ogrino et al. 2016). Moreover, the tropical precipitation is usually due to convection (Dai 2001), tropical convection is also well known to have an important influence on the large-scale atmospheric circulation (Neale and Slingo 2003; Sobel et al. 2011).

Many efforts have been made to understand the mechanisms behind the diurnal precipitation cycle over tropical islands. With CMORPH data and regional climate model simulation, Qian (2008) found that sea-breeze convergence, mountain-valley winds and cumulus merger process are the predominant reasons for the diurnal precipitation cycles while the underrepresentation of islands and terrain results in the precipitation underestimate. Hassim et al. (2016) examined the diurnal cycle of rainfall over New Guinea with a 4-km convection-permitting WRF model. They found the importance of the sea breeze in the initiation of rainfall but focused on large-scale atmospheric properties preferential to the propagation of systems offshore at night. They also

found that orography and the coastline along with gravity waves were beneficial for the longevity and maintenance of the convection systems though they are not the fundamental reasons for the convection initiation.

The diurnal cycle of tropical rainfall is usually poorly captured by most global climate models (GCMs) and even cloud-resolving models (CRMs), owing to model uncertainties in depicting the physical mechanisms that underlie the diurnal precipitation cycle (Yang and Slingo 2001; Qian 2008; Nguyen et al. 2015). Yang and Slingo (2001) found that the deficiency of model's physical parameterizations may be the main reason for the difficulty in capturing the observed phase of diurnal cycle in convection. Diurnal variability is only captured in some places or months where the signals are strong, while at other times, the diurnal signals are captured, but with a large timing error of the maxima and minima. Studies show that the LSB may have different contributions to the diurnal variabilities of precipitation at different places (Keenan et al. 1988; Qian 2008; Wapler and Lane 2012; Chen et al. 2017). Precipitation tends to be initiated by the convergence of land breezes (Wapler and Lane 2012) and sea breezes (Qian 2008) over gulf and island areas respectively. Interactions between land breeze and prevailing wind are likely to produce precipitation over the coast area or tropical islands (Keenan et al. 1988; Chen et al. 2017). Recent studies (Bao et al. 2013; Chen et al. 2016, 2017) also have found that convectively driven cold pools and latent cooling, as well as environmental wind and moisture, may play important roles in the propagation and maintenance of diurnal rainfall in coastal regions. How cold pools and latent cooling affect the diurnal cycle of rainfall and related LSB over a tropical island has not been studied extensively.

This work is aimed at examining the diurnal cycle of precipitation and the related LSB over Hainan Island in the South China Sea. Hainan Island is a tropical island located off the southern

coast of China (Fig.1). It is one of the rainiest areas in China, and is influenced by a variety of synoptic-scale and mesoscale weather systems, such as monsoon, tropical cyclones, LSB, and mountain-plain solenoids. The island's topography features mountains in the southwest, with peak altitude of approximately 1000 meter above the sea level (shaded in Fig. 1), and plains in the northeast.

The characteristics of precipitation and LSB over Hainan Island have been examined via statistical methods based on either surface observation or modeling simulations (Tu et al. 1993; Zhai et al. 1998; Zhang et al. 2014; Liang and Wang 2016). Based on nine station-based wind observations, Zhang et al. (2014) found that LSB occurs more frequently in summer and autumn, though their findings are limited in using observations in only one month of one season. Most recently, Liang and Wang (2016) examined the relationship between the sea breeze and precipitation of Hainan Island using surface wind and precipitation observations along with the global reanalysis over several years. They hypothesized that the seasonal precipitation is due to the initiation of convection by the LSB, but they did not provide thorough investigation on how the LSB circulations trigger and enhance the precipitation over Hainan Island.

The objective of this study is to investigate the diurnal precipitation variation over Hainan Island and the detailed physical mechanisms related to LSB forcing and variability. This is the first time using semi-idealized convection-permitting simulations with climatological mean initial conditions and lateral boundary conditions to study the dynamic and thermodynamic processes (and the impacts of land-sea breeze circulations) that control the rainfall distribution and climatology over a tropical island. We also highlight the removal of terrain effect, along with a further simplification using a perfect oval shaped island. The study relies on rain gauge observations and satellite-derived precipitation estimates, as well as convection-permitting

106 numerical simulations. Section 2 describes the dataset and the methodology. Section 3 documents
107 the diurnal precipitation variation in each month, as well as its fraction of the total precipitation
108 that can be attributed to the diurnal cycle. The relationship between the precipitation and surface
109 winds during the first rainy season [May and June, which is defined relative to the second rainy
110 season (July through September) of southern China when precipitation is mainly caused by
111 typhoons] are also analyzed. The model configuration and results of the simulations are presented
112 in Section 4. Conclusions are presented in Section 5.
113
114 **2. Observation dataset and methodology**
115 Rainfall was analyzed using 19 rain gauges on Hainan Island (Fig. 1). The gauges are
116 relatively evenly distributed across the island. The sampling frequency is one hour, which is dense
117 enough to represent the diurnal precipitation variation over the island. The dataset spans 60 years
118 (1951–2010), though full records exist for only a subset of this period at some of the stations,
119 owing to the fact that the stations were built at different times (the detailed dataset periods for each
120 station are shown in Table 1). Surface temperature and wind observations obtained at the same
121 locations over a four-year period (2007–2010) were used to investigate the land and sea breezes.
122 The surface precipitation observations are augmented by National Oceanic and Atmospheric
123 Administration (NOAA) and Climate Prediction Center Morphing Technique (CMORPH) data
124 derived from low-Earth orbiting and geostationary satellites (Joyce et al. 2004). The CMORPH
125 grid with a temporal resolution of 30 minutes is 0.7277 degree by 0.7277 degree (approximately 8
126 km by 8 km). Ten years of CMORPH data (2006–2015) were used.
127 A series of convection-permitting numerical simulations were performed with the Advanced
128 Research Weather Research and Forecasting (ARW, Skamarock et al. 2008) model version 3.7.1

129 to investigate dynamical features of the diurnal cycle of precipitation and its physical mechanisms
130 in particular with regards to LSB forcing. Initial and lateral boundary conditions were provided by
131 the European Center for Medium-Range Weather forecast Interim (ERA-interim) reanalysis data
132 (Dee et al. 2011) of 0.75° × 0.75° grid spacing. Only one domain was used with 225 × 205 grid
133 points and a horizontal grid spacing of 2 km. A total of 50 vertical levels were used with the model
134 top at 50 hPa. The Yonsei University (YSU) boundary scheme (Hong et al. 2006), Dudhia
135 shortwave radiation (Dudhia 1989), the Rapid Radiative Transfer Model longwave radiation
136 scheme (Iacono et al. 2008), the single-moment 5-class microphysics (Hong et al. 2004), five-layer
137 thermal diffusion land surface and Revised MM5 surface layer schemes were used, while no
138 cumulus parameterization was used in this study.

139 The initial conditions of all simulations were the average of ERA-interim reanalysis data at
140 0000 UTC in May and June of 2006–2015. The lateral boundary conditions were obtained in the
141 same way as the initial conditions, cycled from 0000 to 0600, 1200, and 1800 UTC. Experiment
142 REAL was initiated with the unmodified initial and lateral boundary conditions to simulate the
143 diurnal characteristics. Experiment NoTER is the same as REAL except that the orography over
144 Hainan Island is removed in the initial conditions in order to isolate the influence of the island's
145 terrain. Simplifying the influences of land category and coastline, experiment IDEAL was
146 constructed with an idealized elliptical island to replace the real Hainan Island in the initial
147 condition. The idealized island has a similar size and orientation, and is located at the same place
148 as Hainan Island (Fig. 1), covered with uniform grassland (LU_INDEX=7 in WRF model) while
149 other areas of the model domain are set as ocean. In order to examine the impact of latent
150 heating/cooling on the LSB and related rainfall, sensitivity experiment FakeDry was performed
151 similar to the IDEAL experiment, except for turning off latent heating and cooling in the model

(no_mp_heating=1 in WRF model). Another sensitivity experiment NOVAP was performed similar to IDEAL experiment except for turning off the evaporation of liquid water, which prevents the cold pool generation from moisture convection process. A similar methodology has been used to study diurnal cycle of precipitation in many different regions (Trier et al. 2010; Sun and Zhang 2012; Bao and Zhang 2013; Chen et al. 2016, 2017). The biggest advantage of this method is that it is able to capture the general characteristics of the diurnal cycle of precipitation and the related dynamical processes instead of just focusing on a single case. All simulations were integrated for one month. The mean over the last 26 days was used for the analyses in order to alleviate the spin-up issue and day-to-day variability.

3. Observation analysis

3.1. Diurnal variation of precipitation and its seasonal-dependent features

Diurnal variations of precipitation were examined at each single station in each month based on the hourly gauge precipitation observation averaged over the period from 1951 to 2010. The hourly precipitation evolution shows a significant seasonal cycle over the island. Most of the precipitation falls from April to October, which is the monsoon season, and exhibits a distinct diurnal cycle during that period, whereas less precipitation and lack of a strong diurnal cycle characterize the other months (Fig. 2). The seasonal variability is related to the annual cycle of the East Asian Monsoon. April and September are the two transitional periods of the low-level prevailing wind; the prevailing wind strongly influences the transport of water vapor and precipitation.

The diurnal precipitation cycle has the maximum precipitation at 1500 local standard time (LST, LST=UTC+8) in most months during the warm season, except at 1600 LST in April and

July. No second precipitation peak is observed, which is different from studies of other tropical islands in which a second peak between midnight and early morning has been noted (Kishtawal and Krishnamurti 2001; Wapler and Lane 2012). The second nocturnal peak was found to be closely related to convection caused by mountain-plains solenoid that propagates offshore and coincides with the land breeze during the night or early morning.

The diurnal precipitation cycle shows location-dependent features (Fig. 2). We grouped the stations with different colors based on their similarity in diurnal variations which to a large extent are correlated with their geographical locations. No heavy rainfall or distinct variability is observed at stations along the southern coastline (blue dots on Fig. 1 and blue lines on Fig. 2). All the rest of the island stations share similar diurnal peak precipitation times with the red-dot stations (in red lines) having the highest peak values from April to July while in August and September both the red-dot and black-dot stations (mostly inland) share strongest peaks.

Even though the distribution of gauge-based precipitation station is relatively even across the island, the observations are still too sparse to analyze the detailed rainfall pattern over the island. For this reason, satellite-derived precipitation CMORPH data were also used to examine the diurnal rainfall variation for each of the 19 gauge stations. The hourly diurnal precipitation variation derived from the CMORPH data agrees well with the rain gauge observations in each month (Fig. 3), though the CMORPH amounts are slightly smaller. The time of peak precipitation in the warm season (from May to August) is delayed by one hour in most months in the CMORPH data (maximum at 1600 LST) relative to the peak in the gauge-based observations. These results indicate good agreement between the CMORPH data and gauges, in particular for the warm-season months that are the focus of this study.

197 The fraction of the diurnal precipitation in the total precipitation over the island in each
198 month was examined with the CMORPH data (Fig. 4). Similar to He and Zhang (2010) and Bao
199 et al. (2011), the diurnal precipitation fraction was defined as the mean rainfall rate at each 1-hour
200 interval $=\frac{\sum_{t=0}^{23}|(r_t-\bar{r})|}{r_d}$, in which, r_t is the mean hourly precipitation at each hour t (0–23), $\bar{r}$ is the
201 mean hourly precipitation at all hours, and the r_d is the daily mean precipitation. The diurnal
202 precipitation account for a large fraction of the total precipitation over the island in most months
203 (Fig. 4). In particular, the total precipitation in May is almost entirely attributable to the diurnal
204 cycle (Fig. 4e). The diurnal contribution of the total precipitation exceeds 60% averaged for the
205 whole year and over the whole island, although the magnitude is smaller in September and October.
206 The diurnal precipitation fraction value exceeds 20% in August and September (Figs. 4h and i).
207 Moreover, the area exhibiting a large magnitude of diurnal precipitation roughly coincides with
208 the region also having the most accumulated precipitation. However, the diurnal precipitation
209 fraction is not quite related to the precipitation intensity. The precipitation is extremely light in
210 March and somewhat heavy in September. However, the diurnal precipitation fractions are
211 reversed (smaller fractions in September, greater fractions in March), which is likely related to
212 different physical processes of the precipitation in those months. The detailed physical processes
213 that lead to the steady decrease of diurnal precipitation fraction from May to October before
214 increasing again are beyond the scope of the current study. The possible reasons could be attributed
215 to the synoptic scale storms, typhoons, prevailing winds, the land sea temperature contrast and
216 atmospheric moisture content, which will be explored in our future study**.**
217

218 **3.2. The diurnal cycle of precipitation, land breezes, and sea breezes in May and June**

A more detailed analysis of the diurnal rainfall variation in May and June was carried out because of the intense hourly mean rainfall and high diurnal precipitation fraction. In May, the prevailing warm and wet southwest monsoon airflow transports abundant moisture from the ocean to Hainan Island. A distinct diurnal cycle of precipitation, with a single peak between 1200 and 2000 LST, is evident in both the gauge-based and CMORPH data (Fig. 5). The datasets agree well with each other at each surface station, except that CMORPH data exhibit larger peak values at the red and green stations. Four gauge-based stations in blue have a much weaker daytime peak. These stations, however, have an apparent nocturnal peak, whereas other stations do not exhibit a nocturnal peak. The nocturnal precipitation is possibly attributable to the convergence between the low-level prevailing wind and downhill jet circulations, which are to be examined with the numerical simulations in section 4. The average over all stations (thick black line in Fig. 5) also exhibits an obvious diurnal cycle.

The horizontal distribution of precipitation was analyzed using the CMORPH data (every 3 h except for using 1700 LST as it is the strongest rainfall time in CMORPH data in Fig. 6) along with the perturbation surface wind at gauge stations, which was obtained by subtracting the daily mean from the total wind to highlight the diurnal cycle. The precipitation averaged over all times shows that the precipitation mainly appears in the northeast in the lee-side of mountainous area (Fig. 6a). The gauge-based stations with significant diurnal cycle (in red dots) are located over the heaviest rainfall region while the gauge-based stations with non-distinctive diurnal feature (in blue dots) are located in the weakest precipitation area. Hourly variation of precipitation shows that there is little precipitation over the island in the early to mid-morning (0000 to 0900 LST), which is on average less than that over the surrounding ocean. At 0600 LST, the perturbation surface wind at gauge stations has an offshore direction in coastal area, a signature of nighttime land breeze

242 (Fig. 6b). Three hours later at 0900 LST, the perturbation wind strengthens and turns to the right
243 of its previous direction, particularly along the coast (Fig. 6c). At 1200 LST, the wind has changed
244 to onshore direction representing the beginning of sea breeze, along with the start of weak inland
245 precipitation where the sea breeze converges (Fig. 6d). In the next several hours (Figs. 6e–f), the
246 rainfall intensifies rapidly, reaching to the peak at around 1700 LST. The heaviest precipitation
247 concentrates in the northeast island corresponding to strong convergence of sea breeze (Fig. 6f).
248 The precipitation dissipates rapidly thereafter and there is almost no precipitation by 0300 LST
249 (Figs. 6g–i). The perturbation wind also weakens quickly and turns to offshore along the northern
250 coast. The magnitude of the perturbation wind is close to zero over the island at 2100 LST (Fig.
251 6g). The land breeze intensifies slowly and nocturnal precipitation initiates along the southeast
252 coast of the island (Fig. 6h). The nocturnal precipitation intensifies to the peak and expands to a
253 larger area at 0300 LST, while the precipitation decreases to a minimum (near zero) over the central
254 island (Fig. 6i).

255 Although the analyses on the precipitation and surface wind observation can efficiently
256 reflect general features of the diurnal rainfall variation and the LSB, they cannot be used to
257 examine the detailed dynamics and thermodynamics processes of the diurnal precipitation cycle
258 and the related LSB over the tropical island. The three-dimensional structures of the LSB, as well
259 as the mechanism of how the LSB triggers and enhances the diurnal precipitation cannot be
260 resolved by the surface observation alone. These aspects were examined using a numerical model,
261 as discussed in the next section.

262

263 **4. Numerical simulation results**

264 **4.1. The simulated diurnal cycle and the influence of the orography**

265 The REAL simulation reproduces the diurnal cycle of precipitation and the associated LSB.
266 The diurnal variations of the 2-meter temperature, 2-meter temperature tendency, and precipitation
267 averaged over the last 26 day of the WRF simulations and all stations over the island (Fig. 7) show
268 generally good agreement with the observations except for slightly higher peak values of simulated
269 2-meter temperature and simulated precipitation (cf. Figs. 7a and 7b). The overall process of the
270 diurnal variation over the island was well simulated, suggesting that the chosen setup of WRF-
271 ARW has the ability to capture the radiative effect due to solar insolation well. The surface
272 temperature begins to increase at 0600 LST and peaks at 1300 LST, coincident with the increase
273 of solar heating. With the rainfall evaporation cooling rate becoming larger than the solar heating
274 rate and/or the radiative cooling later on, the temperature starts to decrease thereafter. After sunset,
275 the temperature drops continuously, reaching its minimum near 0600 LST.
276 The horizontal distribution of precipitation averaged in REAL (Fig. 8a), especially the location
277 of the high precipitation area, also has reasonably good agreement with that of the CMORPH data
278 at all hours (Fig. 6a), although the simulated precipitation is somewhat larger. The area of heavy
279 precipitation at the center of the island is well captured by the WRF simulation, although the
280 magnitude is noticeably overestimated. The diurnal precipitation cycle is also well revealed by the
281 variation in the horizontal distribution of the simulated precipitation although with a slightly larger
282 magnitude and a 1-hour delay in peak time. The evolution of the simulated surface perturbation
283 wind (on the second lowest model level for horizontal wind, which is the 0.994-sigma level, about
284 50 meters above the surface) is also consistent with the observation despite some discrepancy in
285 magnitude (Figs. 6 and 8), suggesting that the LSB is well captured as well. However, the evening
286 rainfall along the southern coast is missing, which is likely because the resolution we used in this

study was still too coarse to resolve the convection over the southern coast or the physical process was so complex that the model is unable to represent it for now.

The results of the NoTER simulation (with removal of island orography) are highly consistent with those of REAL in terms of both the magnitude and timing of each variable averaged over the whole analysis period and at all stations (Figs. 7b and c). Similar results are also found in the horizontal distribution features (Fig. 8 and Fig. 9). Neither the pattern nor the magnitude is altered meaningfully between the two simulations. These results suggest that the diurnal cycle characteristics are not sensitive to the orography over Hainan Island, although many previous studies demonstrated that the orography can play an important role in the precipitation over other islands (Sobel et al. 2011; Hassim et al. 2016; Barthlott and Kirshbaum 2013).

In order to simplify the influences of land category and coastline, experiment IDEAL was constructed with an idealized elliptical island to replace the real Hainan Island in the initial condition. The diurnal variation of the 2-meter temperature (blue), 2-meter temperature tendency (red) and hourly accumulated precipitation (green) in IDEAL (Fig. 7d) are nearly identical to those in REAL (Fig. 7b) and the station observation (Fig. 7a) except for their larger magnitudes which could be related to the modified surface land category and the smoothed ellipsoidal coastlines. The diurnal variations of the hourly accumulated precipitation and perturbation wind on the second lowest model level for horizontal wind (Fig. 10) in IDEAL simulation show that the timing of the LSB transitions and the precipitation location are quite similar to those in REAL and the observation with much smoother distribution in the horizontal perturbation wind and precipitation over the island. The relationship between the diurnal variation of precipitation and LSB will be further examined in details based on the results of IDEAL in the next section.

310 **4.2. Diurnal variation of precipitation and the related LSB in IDEAL**

311 The mean fields averaged over all hourly model output times during the last 26 days of the
312 simulation depict a southerly low-level prevailing flow over the whole domain, which transports
313 warm moist air to the island from the South China Sea (Fig. 10a). Greater moisture appears in the
314 northern island over the heavy precipitation area under the influence of southwesterly low-to-mid-
315 level flow (850 hPa, Fig. 11a). Higher surface temperature appears over the southern side than that
316 in the northern side (Fig. 12a).

317 Based on the different phases of surface temperature and perturbation wind, we divided the
318 diurnal cycle process into four stages to elucidate the mechanisms in each stage. The stages are:
319 (1) the establishment of a sea breeze (0600–1200 LST), (2) the peak sea breeze and peak
320 precipitation (1200–1800 LST), (3) the establishment of a land breeze (1800–0000 LST), and (4)
321 the peak land breeze phase (0000–0600 LST). More detailed analyses will be focused on the two
322 middle stages. These are most complicated stages, but are also the most pertinent to the heavy
323 diurnal precipitation (and are therefore most interesting).

324

325 **a. Stage 1. Establishment of a sea breeze (0600–1200 LST)**

326 This stage commences with the onset of surface heating following sunrise. Because ocean and
327 land have different heat capacities, the island is heated faster than the surrounding ocean. The
328 temperature gradient between the island and the surrounding ocean gradually reverses from
329 offshore to onshore, which results in the weakening and demise of land breeze, and the
330 establishment of a sea breeze over the island.

331 In early morning hours when the sun is just about to rise, surface air temperatures over the
332 island attain their lowest readings, with air temperatures being a few degrees lower than over the

surrounding ocean (Fig. 12b). Owing to persistent solar heating, the surface air temperature over most part of the island exceeds the ocean by 0900 LST (Fig. 12c). Meanwhile, the surface air temperature gradient is directed from offshore to onshore, although the land breeze still persists over the island at this time.

The local rate of warming is inhomogeneous over the island. The surface temperature in the northeastern part of the island are considerably lower than that in other regions where the temperatures surpass the surrounding ocean by 0900 LST. The slower warming in the northeastern part of the Hainan Island is likely due to the morning fog or cold pool air (Fig. 13b) that commonly forms within the area humidified (Fig. 14b) by late-afternoon precipitation on the preceding day. The cloud over the area attenuates solar radiation and subsequently slows the local warming. Moreover, positive horizontal temperature advection exists over the southern island (Fig. 15a and b), which helps to increase the temperature faster over the area. The sea breeze begins to develop along the southwestern coastline owing to the weakest land breeze and the highest warming rate, while other areas of the island are still under the control of the land breeze with an offshore temperature gradient (Fig. 12c). Two land breeze circulations (LBCs) appear clearly in the vertical direction below 3 km along the coast of the island at 0600 LST (Fig. 14b). The southern LBC recedes quickly with the reversal of the temperature gradient at around 0900 LST, while the other LBC remains distinct (Fig. 14c).

By 1200 LST, the temperature gradient reverses to the onshore direction, while the sea breeze has fully established along the entire coastal line (Fig. 12d). Unevenly warming speeds over the island with much more rapid warming over the north while slower warming over the south, which is a result of a high negative horizontal temperature advection over the southern island along the coastlines (Fig. 15d). A sea-breeze front appears at the leading edge of the sea breeze along the

356 coastline, particularly along the northernmost coast where the maximum near-surface temperature
357 gradient lies (Fig. 12d). At the same time, copious water vapor is transported inland from the ocean
358 owing to the low-to-mid level prevailing wind (Fig. 11d) and upward motions (Fig. 14d). Clouds
359 initially form along the sea-breeze (Fig. 13c) and subsequently produces rainfall (shaded in Fig.
360 10d and green lines in Fig. 13d). Noticeably, more rapid warming during this period happens over
361 the northwest of the island while it is much slower over the other areas (Fig. 12d), which is because
362 of the horizontal gradient and advection of the temperature over the whole island (Fig. 15).
363
364 **b. Stage 2. Peak sea breeze and peak precipitation (1200–1800 LST)**
365 Surface temperature is a maximum from 1200 to 1400 LST over most of the island, then
366 decreases rapidly thereafter owning primarily to the development of precipitation (which has its
367 diurnal maximum during this period) and associated evaporative cooling. Besides, surface
368 temperature is also controlled by other processes, such as surface heat fluxes, both shortwave and
369 long wave radiative processes, diffusion in the soil, etc. The sea breeze also reaches its peak
370 intensify in the 1200-1400 LST time period.
371 At 1500 LST, surface temperature decreases over the rainfall area owing to evaporation
372 cooling and slightly increases over other areas because of continuous solar heating (Fig. 12e).
373 There is significant enhancement in upward motions in the low to middle troposphere (Fig. 14e).
374 The sea breeze reaches its peak strength and greatest inland penetration (Fig. 12e). Two distinct
375 sea breeze circulations (SBCs) are clearly seen in the vertical cross section, with the stronger one
376 over the northern flank of the island (Fig. 14e). Moisture air is transported from ocean to the island
377 persistently by the deep southwesterly prevailing wind throughout the lower troposphere (Fig. 11e)
378 while low-level convergence of moisture air generating strong updraughts, which results in an

379 increase of the moisture over the midlevels (Fig.14e). These factors favor the development of deep
380 convection over the northern flank of the island. As a result, precipitation increases significantly
381 along the sea breeze front (Fig. 10e).

382 By 1800 LST, the strongest rainfall falls over the island (Fig. 10f) owning to strongest low-
383 level convergence and subsequent lifting of warm moist air (Fig. 14f). The sea breeze fronts move
384 further inland and collide with each other near the center of the island (Fig. 12f), with a deep layer
385 of moisture over the northern side of the island that fuels the strong precipitation (Figs. 11f and
386 14f). Cold pools form due to the evaporation cooling of the precipitation, contributing to the
387 propagation and enhancement of the precipitation, which will be further examined with two other
388 sensitivity experiments in the next part. The precipitation pattern (Fig. 10f) exhibits a horseshoe
389 shape aligned with the prevailing wind direction, which is similar to the result of the urban heat
390 island study by Han and Baik (2008).

391

392 **c. Stage 3. Establishment of a land breeze (1800–0000 LST)**

393 During this period, the convection quickly dissipates and the sea breeze is replaced by a land
394 breeze (Figs. 10g and h) after sunset. The surface temperature decreases continuously throughout
395 this stage over the island. The rate of temperature decrease is fastest in the first several hours,
396 reaching around -1.5 K h^{-1} at 1800-1900 LST (red line in Fig. 7d) due to the sudden loss of solar
397 heating. The horizontal temperature gradient begins to reverse, which eventually leads to the
398 establishment of the land breeze (Figs. 12g and h). By 2100 LST, approximately two hours after
399 sunset, temperature over the island is decreasing rapidly both at the surface (Fig. 12g) and
400 throughout the boundary layer. Meanwhile, subsidence becomes dominant over the island (Fig.

401 14g). The subsidence dries the lower levels and rainfall has ceased over the whole island (Fig.
402 13g).

403 By 0000 LST, with the continuous decreasing of temperature and amplifying of the offshore
404 temperature gradient, the land breeze circulations are well established in particular across the shore
405 of the northern island (Fig. 14h). Further drying is seen in mid-to-low levels as the much stronger
406 downward flow occurs over the island, which transports dry air from aloft to the mid-to-low levels
407 (Figs. 11h and 14h). At the same time, under the influence of the prevailing wind, much more
408 moisture air is concentrated over the northern island, so the moisture over the northern island is
409 much moister than the southern island. Clouds vanish quickly and precipitation dissipates almost
410 completely by this time.

411

412 **d. Stage 4. Peak land breeze (0000–0600 LST)**

413 The land breeze reaches its maximum intensity during this period. Nighttime radiative cooling
414 results in the minimum temperature being attained at approximately 0500 LST. From 0000 to 0300
415 LST, the land breeze intensifies rapidly along the northwest coast, becoming nearly perpendicular
416 to the coastline and parallel with the low-level prevailing wind as the surface temperature over
417 land decreases (Fig. 12i). Two LBCs are evident in the vertical cross section (Fig. 13i). Subsidence
418 extends over the entire island (Fig. 14i). The peak land breeze is established at 0600 LST (Fig.
419 12b). The strong subsidence also leads to further midlevel drying (Fig. 11b). Near the surface, the
420 cooling is associated with an increase in the relative humidity, which induces the formation of low
421 clouds and fog (Fig. 13b).

422

423 **4.3. The impacts of latent heating/cooling on LSB and the related rainfall**

Surface temperature in the FakeDry experiment agrees well with the IDEAL over the island, which indicates that the solar heating rather than the latent heating/cooling is primarily responsible for the temperature variability. Although the precipitation is decreased significantly, light rainfall still occurs in the late afternoon in conjunction with the sea breeze front, but with an approximate 3-h delay in convective initiation. The precipitation attains its maximum at 1800 LST, which along with the peak sea breeze, also lags that in the IDEAL experiment by approximately three hours.

The impact of cold pool and latent cooling on the sea breeze and rainfall was further examined using the Hovmöller diagrams of zonal wind perturbations on the second lowest model level for horizontal wind and hourly precipitation along the red line in Fig. 1 for experiments IDEAL, FakeDry and NOVAP (Fig. 16). A weaker sea breeze is observed in the FakeDry experiment than in the IDEAL experiment while NOVAP experiment shows the strongest sea breeze. The NOVAP experiment generated much stronger precipitation over the island as the rain evaporation cooling process was turned off. The propagation of the LSB is much slower and the inland propagation distance is much shorter in FakeDry experiment than that in the IDEAL experiment while the propagation speed in NOVAP experiment is between the other two experiments, which suggests that cold pool can accelerate the precipitation over the tropical island. In the NOVAP experiment, the heavy precipitation does not dissipate after 2100 LST but propagates into the northeast out of the island with the land breeze, indicating that cold pool plays an important role in dissipating the convection. Moreover, given precipitation varies precisely with the convergence and divergence of horizontal winds due to LSB in all simulations, it is evident that the LSB is the primarily forcing for the diurnal precipitation variability over the island.

The LSB circulations in the FakeDry experiment are similar to those in the IDEAL experiment, and consistent with the NOVAP experiment, except that they are confined to lower levels (around

447 2 km) owing to weaker vertical motion [Strong vertical velocities extend to altitudes exceeding 5
448 km in the IDEAL experiment, whereas they only extend to 2 km in the FakeDry experiment (not
449 shown).] The latent heating can strengthen vertical movement and extend the LSB circulations to
450 higher altitudes. The latent heating feedback can also lead to stronger and earlier convection
451 initiation and precipitation along the sea breeze fronts. In turn, the cold pool further promotes the
452 inland penetration of the sea-breeze front and dissipates the precipitation (Fig. 16), which is
453 because the pressure gradient increases and drives the sea breeze flow more inland when cold pool
454 moves toward the island/inland.
455
456 **5. Summary**
457 Diurnal cycle of precipitation over tropical areas is poorly captured by numerical models,
458 owing to model uncertainties in depicting the physical mechanisms that underlie the diurnal
459 precipitation cycle, which is considered to be closely linked with the land-sea breeze. This study
460 explored the diurnal precipitation variation and its relationship with the land/sea breeze
461 circulations on Hainan Island, a tropical island located off the southern coast of China, based on
462 gauge observation and satellite-estimated precipitation, as well as convection-permitting
463 numerical simulations. The diurnal cycle of precipitation in each month over the island was
464 analyzed with 19 gauge observations during 1951–2010. Most precipitation falls during warm
465 season (from April to October) and exhibit a significant diurnal cycle, whereas much lesser
466 precipitation fall in other months. Precipitation is at a maximum between 1500–1700 LST in the
467 warm season at almost all stations except for four stations along the southern coastline of the island.
468 The satellite-derived CMORPH precipitation estimates from 2006–2015 were further used to
469 validate the diurnal precipitation variation. The CMORPH data agrees well with gauge observation

except for a smaller magnitude of precipitation and a 1-hour delay in the timing of the daily precipitation maximum during the warm season. The analysis of CMORPH data shows that about 60% of the total annual precipitation over the island is attributable to diurnal variations, with the largest proportion in May and the smallest proportion in September and October. For May and June, precipitation begins around local noon time, intensifying quickly thereafter, and reaching a peak at ~1500 LST based on station observations. This diurnal rainfall cycle is, for the most part consistent with the diurnally varying low-level wind convergence and divergence.

A series of numerical simulations (REAL, NoTER, IDEAL, FakeDry and NOVAP) using a convection-permitting configuration of the WRF model (2-km horizontal grid spacing) were conducted to understand the underlying mechanisms of the diurnal precipitation variations. The initial and lateral boundary conditions were generated using a 10-year (2006–2015) average of ERA-interim data for May and June. Results show that the orography of Hainan Island may be of only secondary influence on the diurnal precipitation cycle, which is different from past studies on other hilly islands. Similar diurnal cycles of precipitation and related land/sea breeze circulations were simulated between simulations with and without orography over the island. Even with an idealized elliptical and flat island covered by only grassland, located at the same place with similar area and orientation, the diurnal cycle characteristics can still be fairly well captured. Those results show that: (1) WRF is capable of replicating the important aspects of the mean diurnal cycle compared to rainfall observations, (2) removing the orography and coastal features made little difference to the diurnal cycle during the rainiest times of the year, (3) the dominant process that produces the diurnal cycle were shown to be the sea/land breezes caused by the relative surface heating/cooling of the island compared to the surrounding ocean, and (4) evaporative cooling as part of convective systems also plays an important role in the diurnal cycle.

493 The simulated diurnal cycle of precipitation and related land/sea breeze circulations based on
494 the idealized flat-island simulation were divided into four stages in terms of the evolutions of
495 temperature, winds and precipitation. Stage 1 is from 0600 to 1200 LST, during which time the
496 land breeze is replaced by a sea breeze as solar heating warms the interior of the island. Abundant
497 moisture is transported to the low to middle troposphere over the island, resulting in convective
498 initiation and precipitation along the sea-breeze front. Stage 2 is from 1200 to 1800 LST, during
499 which time sea breeze attains to its peak intensity and precipitation is a maximum. The sea breezes
500 from opposite sides of the island eventually penetrate all the way to the island's center and collide,
501 which results in the maximum precipitation being located there. Stage 3 is from 1800 to 0000 LST,
502 during which time a land breeze is established as a result the cooling over the island. The cooling
503 is due primarily to the sudden loss of solar heating. Subsidence from the land breeze prevents
504 further precipitation by early evening. The last stage covers the peak of the land breeze, which is
505 observed near sunrise.

506 The FakeDry and NOVAP experiments show that the latent cooling and cold pool have a small
507 impact on the land/sea breeze circulations but can apparently enhance precipitation. Strong
508 convection can enhance the sea breeze, and the augmentation of the sea breeze by the evaporatively
509 driven cold pool helps to accelerate the inland propagation of the sea breeze and weakens the
510 convection.

511 Finally, it is worth mentioning that the 1-hour delay in the timing of the maximum
512 precipitation in the simulation is probably caused by the 2-km horizontal resolution, which may
513 not be high enough to resolve explicit underlying physical processes. It is likely for the same reason
514 that the weak nocturnal precipitation is not captured by the simulations. Much higher horizontal
515 and vertical resolution might be needed in the future work to resolve more detailed processes

related to the diurnal cycles. On the other hand, there are many other factors like biases in ERA-Interim reanalysis data used for the initial and boundary conditions to drive the numerical simulations and biases in physical processes (microphysics, surface processes, radiative process, etc), which will be studied in follow-on work. Moreover, the rainfall for different seasons shows quite different patterns, owing to various underlying dynamic and thermodynamic physics. In addition to May and June that were mainly examined in this current work, the diurnal rainfall variation in other months needs to be explored in further studies.

Acknowledgments: Lei Zhu is supported by the Natural Science Foundation of China Grant 41461164006, and the Chinese Scholarship Council (CSC). Zhiyong Meng is supported by the Natural Science Foundation of China Grants 41461164006, 41425018 and 41375048. Fuqing Zhang is supported by the Office of Naval Research Grant N000140910526 and the National Science Foundation Grant AGS-1305798. Paul Markowski is supported by National Science Foundation grant AGS-1536460 and National Oceanic and Atmospheric Administration awards NA15NWS4680012 and NA14NWS4680015. The simulations were performed on the Stampede supercomputer of the Texas Advanced Computing Center (TACC). All data are freely available from sources indicated in the text or from the corresponding author upon request (Email: zymeng@pku.edu.cn).

References

Bao, X., Zhang, F. and Sun, J., 2011. Diurnal variations of warm-season precipitation east of the Tibetan Plateau over China. *Monthly Weather Review*, *139*(9), pp.2790–2810.

Bao, X. and Zhang, F., 2013. Impacts of the mountain-plains solenoid and cold pool dynamics on the diurnal variation of warm-season precipitation over northern China. *Atmos. Chem. Phys*, *13*, pp.6965–6982.

Barthlott, C., and D. J. Kirshbaum, 2013: Sensitivity of deep convection to terrain forcing over Mediterranean islands. *Q. J. R. Meteorol. Soc*., *139*, pp.1762–1779.

Chen, X., Zhang, F. and Zhao, K., 2016. Diurnal Variations of the Land–Sea Breeze and Its Related Precipitation over South China. *Journal of the Atmospheric Sciences*, *73*(12), pp.4793–4815.

Chen, X., Zhang, F. and Zhao, K., 2017. Influence of Monsoonal Wind Speed and Moisture Content on Intensity and Diurnal Variations of the Mei-yu Season Coastal Rainfall over South China. *Journal of the Atmospheric Sciences*, *in review*.

Crosman, E.T. and Horel, J.D., 2010. Sea and lake breezes: a review of numerical studies. *Boundary-layer meteorology*, *137*(1), pp.1–29.

Dai, A., 2001. Global precipitation and thunderstorm frequencies. Part I: Seasonal and interannual variations. *Journal of climate*, *14*(6), pp.1092-1111.

Dee, D.P., Uppala, S.M., Simmons, A.J., Berrisford, P., Poli, P., Kobayashi, S., Andrae, U., Balmaseda, M.A., Balsamo, G., Bauer, P. and Bechtold, P., 2011. The ERA‐Interim reanalysis: Configuration and performance of the data assimilation system. *Quarterly Journal of the royal meteorological society*, *137*(656), pp.553–597.

Dudhia, J., 1989. Numerical study of convection observed during the winter monsoon experiment using a mesoscale two-dimensional model. *Journal of the Atmospheric Sciences*, *46*(20), pp.3077-3107.

Han, J.Y. and Baik, J.J., 2008. A theoretical and numerical study of urban heat island–induced circulation and convection. *Journal of the Atmospheric Sciences*, *65*(6), pp.1859–1877.

Hassim, M.E.E., Lane, T.P. and Grabowski, W.W., 2016. The diurnal cycle of rainfall over New Guinea in convection-permitting WRF simulations. *Atmos. Chem. Phys*, *16*(1), pp.161–175.

He, H. and Zhang, F., 2010. Diurnal variations of warm-season precipitation over northern China. *Monthly Weather Review*, *138*(4), pp.1017–1025.

Hong, S.Y., Dudhia, J. and Chen, S.H., 2004. A revised approach to ice microphysical processes for the bulk parameterization of clouds and precipitation. *Monthly Weather Review*, *132*(1), pp.103–120.

Hong, S.Y., Noh, Y. and Dudhia, J., 2006. A new vertical diffusion package with an explicit treatment of entrainment processes. *Monthly Weather Review*, *134*(9), pp.2318–2341.

Huffman, G.J., Bolvin, D.T., Nelkin, E.J., Wolff, D.B., Adler, R.F., Gu, G., Hong, Y., Bowman, K.P. and Stocker, E.F., 2007. The TRMM multisatellite precipitation analysis (TMPA): Quasi-global, multiyear, combined-sensor precipitation estimates at fine scales. *Journal of Hydrometeorology*, *8*(1), pp.38–55.

Iacono, M.J., Delamere, J.S., Mlawer, E.J., Shephard, M.W., Clough, S.A. and Collins, W.D., 2008. Radiative forcing by long□lived greenhouse gases: Calculations with the AER radiative transfer models. *Journal of Geophysical Research: Atmospheres*, *113*(D13).

Joyce, R.J., Janowiak, J.E., Arkin, P.A. and Xie, P., 2004. CMORPH: A method that produces global precipitation estimates from passive microwave and infrared data at high spatial and temporal resolution. *Journal of Hydrometeorology*, *5*(3), pp.487–503.

Keenan, T.D., Holland, G.J., Manton, M.J. and Simpson, J., 1988. TRMM ground truth in a monsoon environment: Darwin, Australia. *Australian Meteorological Magazine*, *36*(2), p.81.

Kishtawal, C.M. and Krishnamurti, T.N., 2001. Diurnal variation of summer rainfall over Taiwan and its detection using TRMM observations. *Journal of Applied Meteorology*, *40*(3), pp.331-344.

Liang, Z. and Wang, D., 2016. Sea breeze and precipitation over Hainan Island. *Quarterly Journal of the Royal Meteorological Society*.

Mapes, B.E., Warner, T.T. and Xu, M., 2003. Diurnal patterns of rainfall in northwestern South America. Part III: Diurnal gravity waves and nocturnal convection offshore. *Monthly Weather Review*, *131*(5), pp.830–844.

Neale, R. and Slingo, J., 2003. The maritime continent and its role in the global climate: A GCM study. *Journal of Climate*, *16*(5), pp.834–848.

Nguyen, H., Protat, A., Kumar, V., Rauniyar, S., Whimpey, M. and Rikus, L., 2015. A regional forecast model evaluation of statistical rainfall properties using the CPOL radar observations in different precipitation regimes over Darwin, Australia. *Quarterly Journal of the Royal Meteorological Society*, *141*(691), pp.2337–2349.

Ogino, S.Y., Yamanaka, M.D., Mori, S. and Matsumoto, J., 2016. How Much is the Precipitation Amount over the Tropical Coastal Region?. *Journal of Climate*, *29*(3), pp.1231–1236.

Qian, J.H., 2008. Why precipitation is mostly concentrated over islands in the Maritime Continent. *Journal of the Atmospheric Sciences*, *65*(4), pp.1428–1441.

Skamarock, W.C., Klemp, J.B., Dudhia, J., Gill, D.O., Barker, D.M., Duda, M.G., Huang, X.Y., Wang, W. and Jordan, G., *Powers. 2008. A Description of the Advanced Research WRF Version 3. NCAR Technical Note*. NCAR/TN–475+ STR.

Sobel, A.H., Burleyson, C.D. and Yuter, S.E., 2011. Rain on small tropical islands. *Journal of Geophysical Research: Atmospheres*, *116*(D8).

Sun, J. and Zhang, F., 2012. Impacts of mountain–plains solenoid on diurnal variations of rainfalls along the mei-yu front over the east China plains. *Monthly Weather Review*, *140*(2), pp.379–397.

Trier, S.B., Davis, C.A. and Ahijevych, D.A., 2010. Environmental controls on the simulated diurnal cycle of warm-season precipitation in the continental United States. *Journal of the Atmospheric Sciences*, *67*(4), pp.1066–1090.

Tu, X., Zhou, M.Y., Z. and Sheng, S.H., 1993. The mesoscale numerical simulation of the flow field of the Hainan Island and the Leizhou Peninsula. *Acta Oceanolog (in Chinese)*, *12*(2), pp.219–235.

Wapler, K. and Lane, T.P., 2012. A case of offshore convective initiation by interacting land breezes near Darwin, Australia. *Meteorology and Atmospheric Physics*, *115*(3–4), pp.123–137.

Yang, G.Y. and Slingo, J., 2001. The diurnal cycle in the tropics. *Monthly Weather Review*, *129*(4), pp.784–801.

Zhai, W., Li, G., Sun, B. and Dang, R., 1998. Varying season's mesoscale wind field circulation in Hainan island. J. Trop. Meteorol. 4: 79–87.

Zhang, Y., Zhang, F. and Sun, J., 2014. Comparison of the diurnal variations of warm-season precipitation for East Asia vs. North America downstream of the Tibetan Plateau vs. the Rocky Mountains. *Atmospheric Chemistry and Physics*, *14*(19), pp.10741–10759.

Figure Captions

FIG. 1. Configuration of model domain, gauge-based station points (color dots correspond to the time series shown in Fig. 2) over Hainan Island and the terrain height (shading, m). The red ellipse is the idealized representation of the island (used for the idealized simulations), and the red vertical line indicates the location of the vertical cross-sections shown in Figs. 14 and 16.

FIG. 2. Average rainfall accumulations by hour, each month of the year, obtained from the rain gauge network. The color is consistent with the color dots over the island in Fig. 1. LST means the Local Standard Time.

FIG. 3. Average station rainfall accumulations obtained from gauges (blue) and CMORPH (red) in each month.

FIG. 4. Fraction of the total precipitation that can be attributed to the diurnal cycle, by month (shading), along with average hourly precipitation accumulations (black contours every 0.05 mm, starting at 0.25 mm).

FIG. 5. Average rainfall accumulations by hour in May and June (a) from rain gauges and (b) derived from CMORPH.

FIG. 6. Ten-year average, hourly rainfall accumulations at 3-h intervals for May and June derived from CMORPH (shading) except used 1700 LST as it is the strongest rainfall time in CMORPH observation. Three-year average wind velocity (vectors) is also shown. Rain gauge locations are indicated in (a).

FIG. 7. The average of 2-meter temperature (T2_avg), 2-meter temperature tendency (T2_tendency, temperature difference between two neighboring hours), and hourly rainfall accumulation over the island based on (a) gauge observations, (b) simulation REAL, (c) simulation NoTER, (d) and simulation IDEAL. Horizontal colored lines indicate means over all hours.

FIG. 8. Hourly precipitation accumulation (shading) and average perturbation wind (vectors) on the second lowest model level for horizontal wind in simulation REAL every 3 h. The averages over all hours are shown in (a).

FIG. 9. As in FIG. 8, but for simulation NoTER.

FIG. 10. As in FIG. 8, but for simulation IDEAL.

FIG. 11. Water vapor mixing ratio (shading) and horizontal wind (vectors) at 850 hPa, and hourly precipitation accumulations > 0.1 mm (thick purple contours), (b–i) every 3 h and (a) averaged over all times.

FIG. 12. (a) 2-meter mean temperature (shading) and horizontal wind (vectors) on the second lowest model level for horizontal wind; (b–i) 2-meter mean temperature perturbation (shading)

and mean perturbation horizontal wind (vectors) on the second lowest model level every 3 h. The right color bar is used for (a).

FIG. 13. Cloud water mixing ratio (red shading), 2-meter temperature (grey shaded), perturbation horizontal wind on the second lowest model level for horizontal wind (yellow vectors), and hourly precipitation accumulation (green contour lines) every 3 h.

FIG. 14. Vertical cross-sections of relative humidity (shading), perturbation wind (vectors; the scale of the vertical component is increased by a factor of 5), and temperature (contours) in the south-to-north direction (see red line in Fig. 1) averaged over all hours (a) and at 3-h intervals (b–i). The triangles in each panel indicate the edges of the island.

FIG. 15. Horizontal temperature advection (shaded) and horizontal wind (vector, m s^{-1}) on the first model level in simulation IDEAL.

FIG. 16. Hovmoller diagrams of perturbation meridional wind component on the second lowest model level for horizontal wind (shading) in the (a) IDEAL, (b) Fakedry and (c) NOVAP simulations, respectively. Precipitation exceeding 0.1 mm h^{-1} is enclosed by the heavy purple contours. The two vertical dash lines indicate the edges of the island.

Table 1

Station observation period used over Hainan Island

Station No.	Latitude	Longitude	Height (m)	Obs period(YearMonth)	Name
59757	20	110.37	9.9	197701-201212	Qiongshan
59758	20	110.25	63.5	195101-201212	Haikou
59838	19.1	108.62	7.6	195506-201212	Dongfang
59842	19.9	109.68	31	196201-201212	Lingao
59843	19.73	110	31.4	195901-201212	Dengmai
59845	19.52	109.58	169	195505-201212	Zanzhou
59847	19.27	109.05	98.1	196605-201212	Changjiang
59848	19.23	109.43	215.6	196201-201212	Baisha
59849	19.03	109.83	250.9	195602-201212	Qiongzhong
59851	19.7	110.33	24.2	196301-201212	Dingan
59854	19.37	110.1	118.3	196301-201212	Tunchang
59855	19.23	110.47	24	195509-201212	Qiaonghai
59856	19.62	110.75	21.7	195901-201212	Wenchang
59940	18.75	109.17	155	196202-201212	Ledong
59941	18.77	109.52	328.5	196301-201212	Wuzhishan
59945	18.65	109.7	68.6	196509-201212	Baoting
59948	18.22	109.58	419.4	196201-201212	Sanya
59951	18.8	110.33	39.9	196201-201212	Wanning
59954	18.5	110.03	13.9	195601-201212	Lingshui

Figures

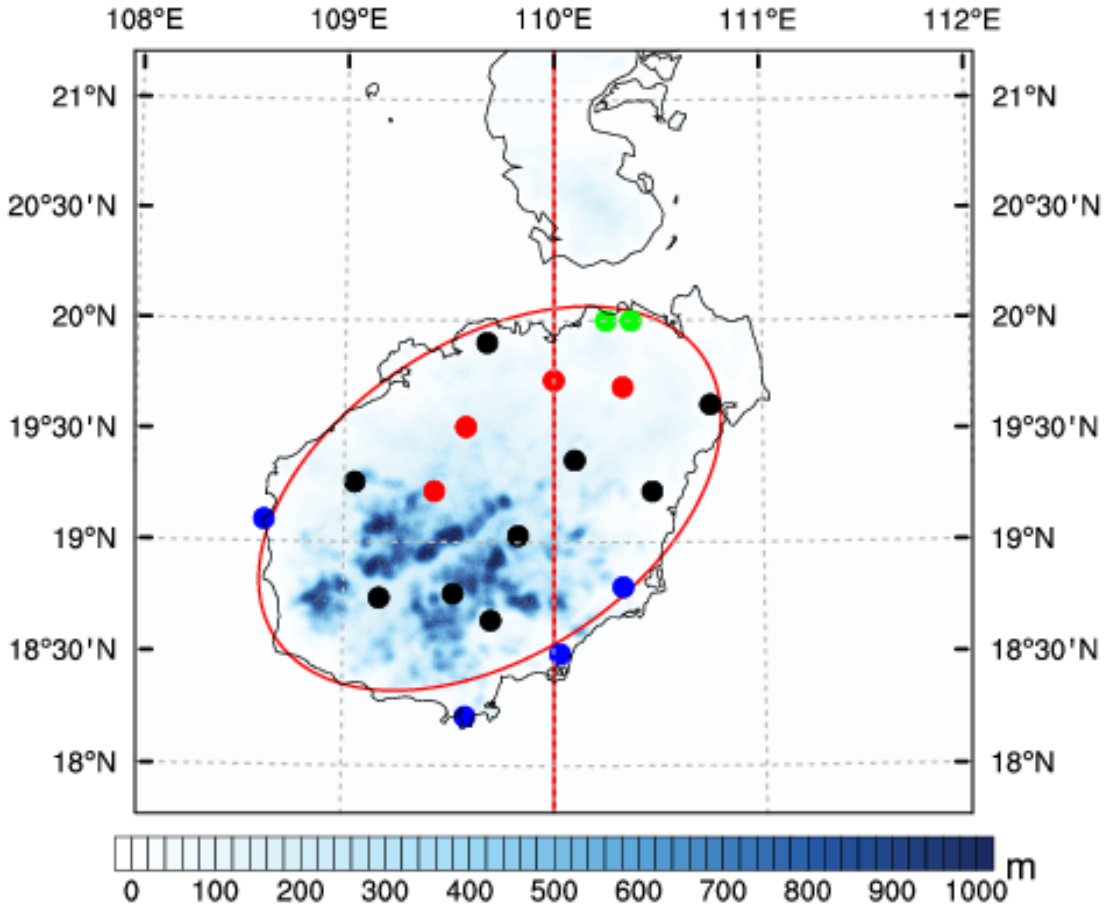

FIG. 1. Configuration of model domain, gauge-based station points (color dots correspond to the time series shown in Fig. 2) over Hainan Island and the terrain height (shading, m). The red ellipse is the idealized representation of the island (used for the idealized simulations), and the red vertical line indicates the location of the vertical cross-sections shown in Figs. 14 and 16.

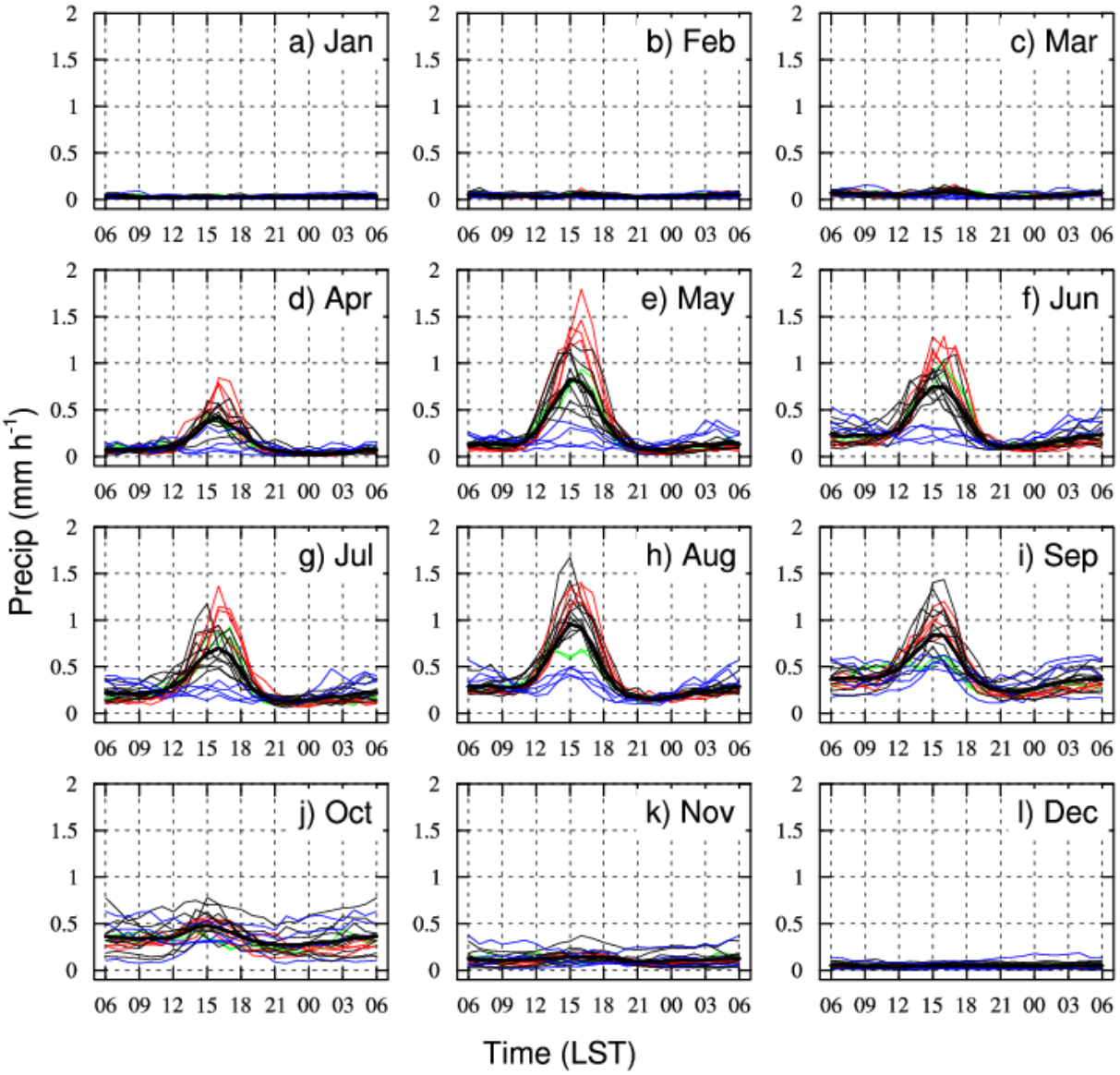

FIG. 2. Average rainfall accumulations by hour, each month of the year, obtained from the rain gauge network. The color is consistent with the color dots over the island in Fig. 1. LST means the Local Standard Time.

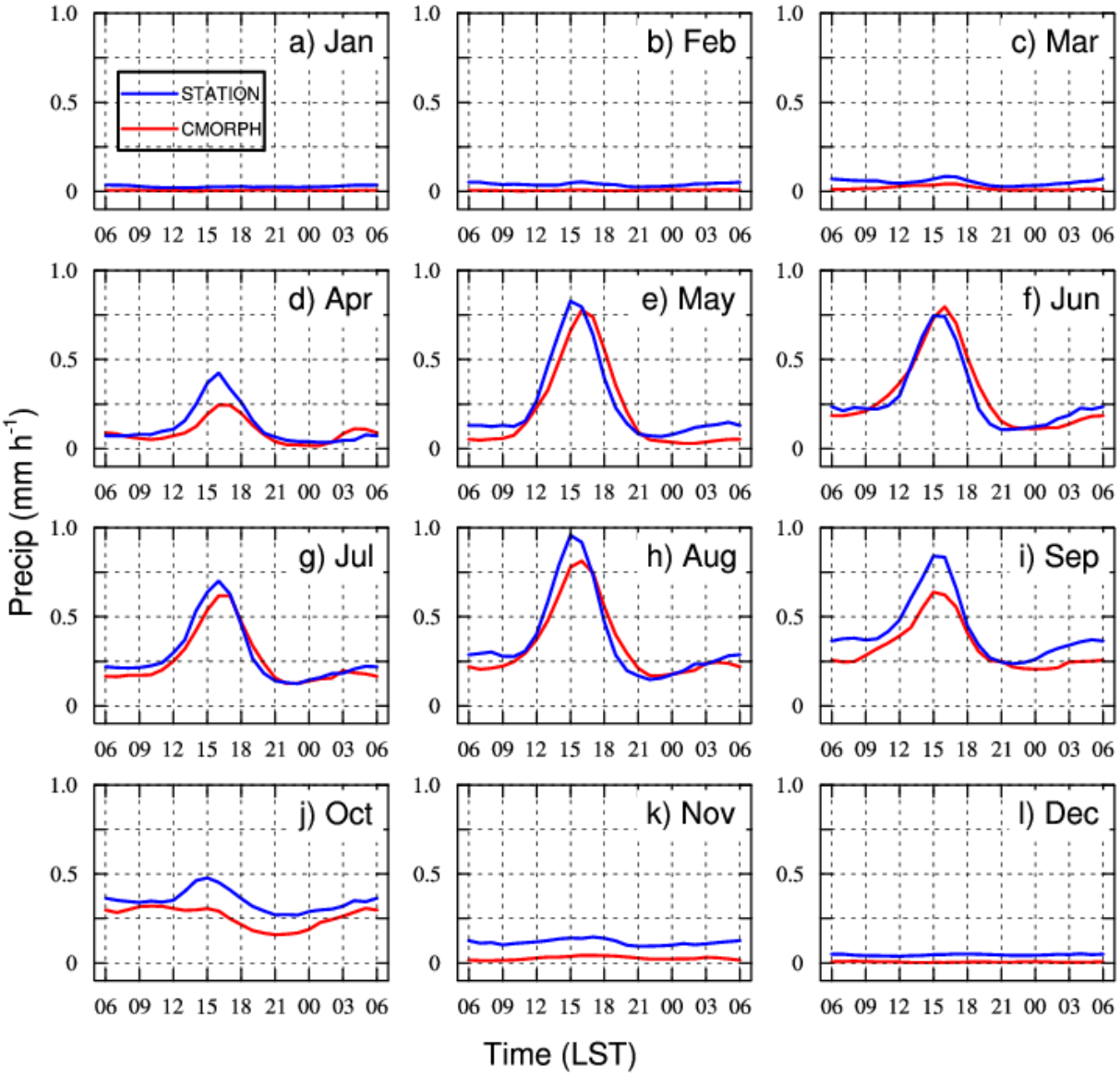

FIG. 3. Diurnal cycles of hourly average rainfall accumulations obtained from gauges (blue) and CMORPH (red) in each month.

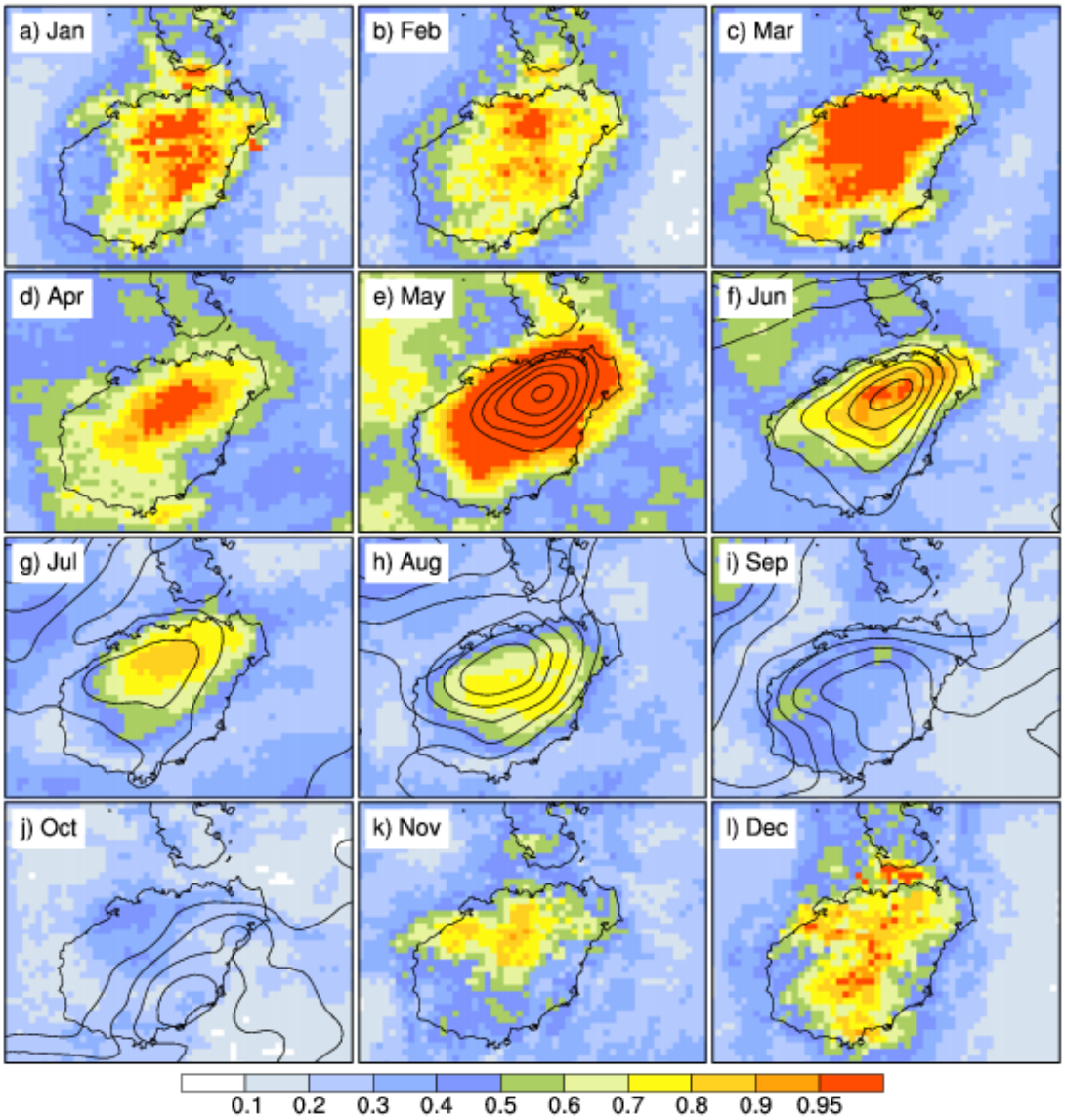

FIG. 4. Fraction of the total precipitation that can be attributed to the diurnal cycle, by month (shading), along with average hourly precipitation accumulations (black contours every 0.05 mm h^{-1}, starting at 0.25 mm h^{-1}).

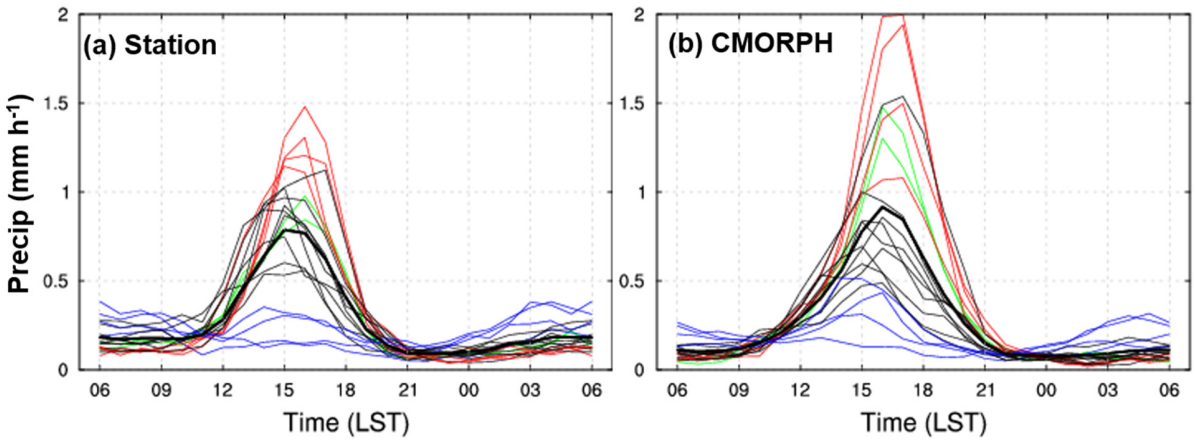

FIG. 5. Average rainfall accumulations by hour in May and June (a) from rain gauges and (b) derived from CMORPH.

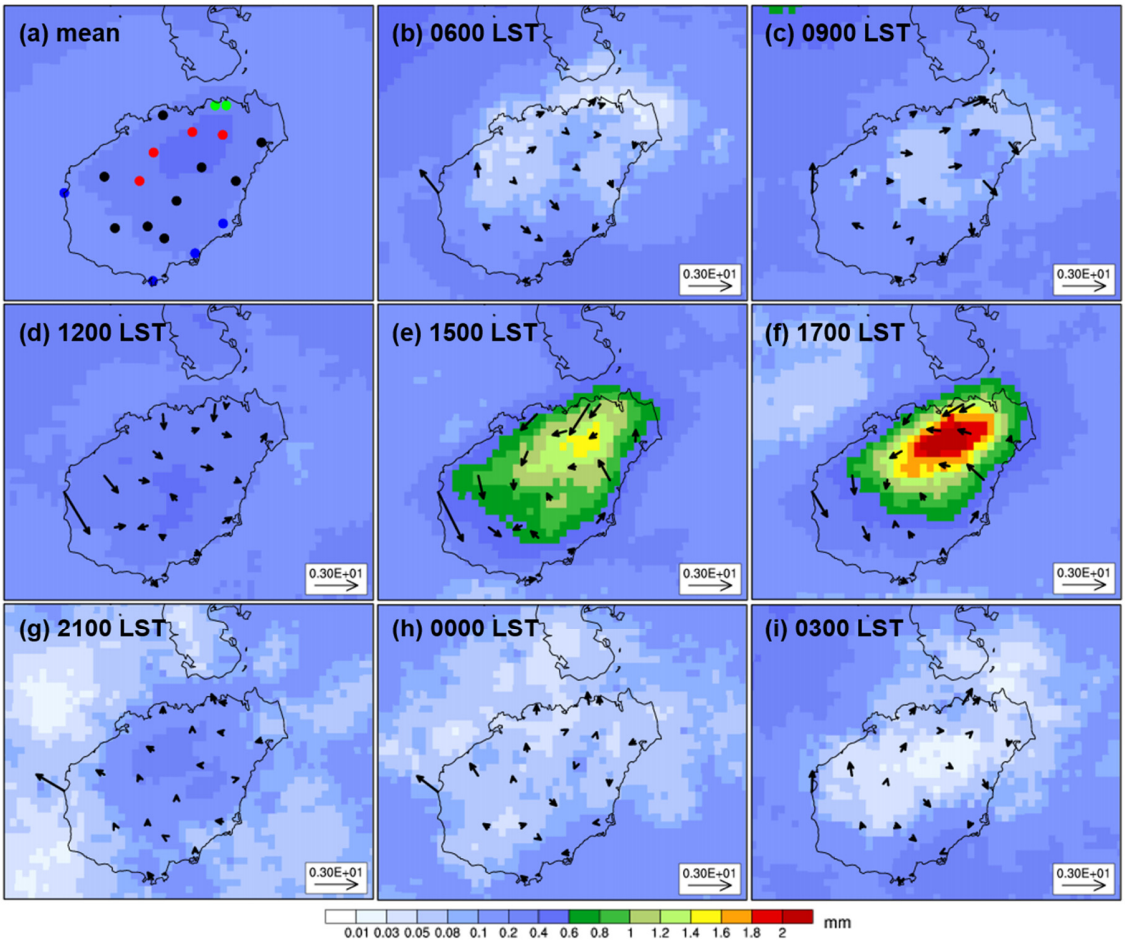

FIG. 6. Ten-year average, hourly rainfall accumulations at 3-h intervals for May and June derived from CMORPH (shading) except used 1700 LST as it is the strongest rainfall time in CMORPH observation. Three-year average wind velocity (vectors) is also shown. Rain gauge locations are indicated in (a).

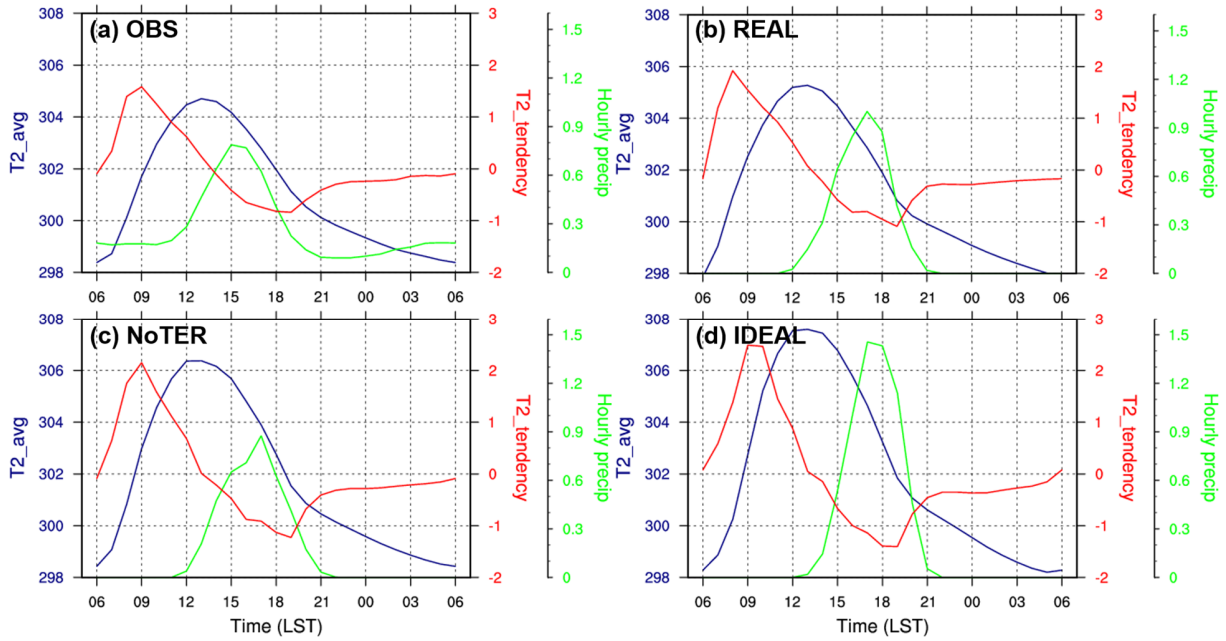

FIG. 7. The average of 2-meter temperature (T2_avg), 2-meter temperature tendency (T2_tendency, temperature difference between two neighboring hours), and hourly rainfall accumulation over the island based on (a) gauge observations, (b) simulation REAL, (c) simulation NoTER, (d) and simulation IDEAL.

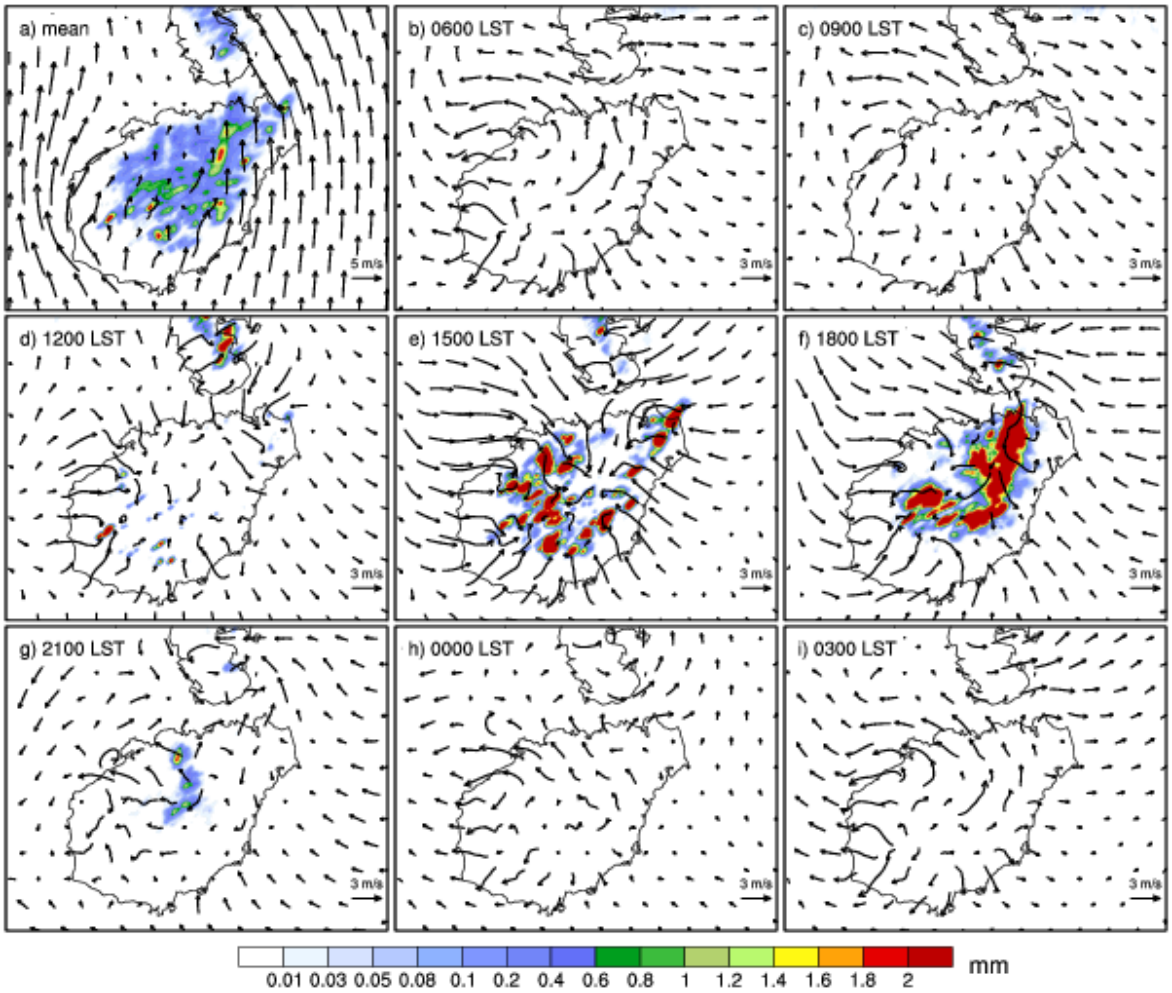

FIG. 8. Hourly precipitation accumulation (shading) and average perturbation wind (vectors) on the second lowest model level for horizontal wind in simulation REAL every 3 h. The averages over all hours are shown in (a).

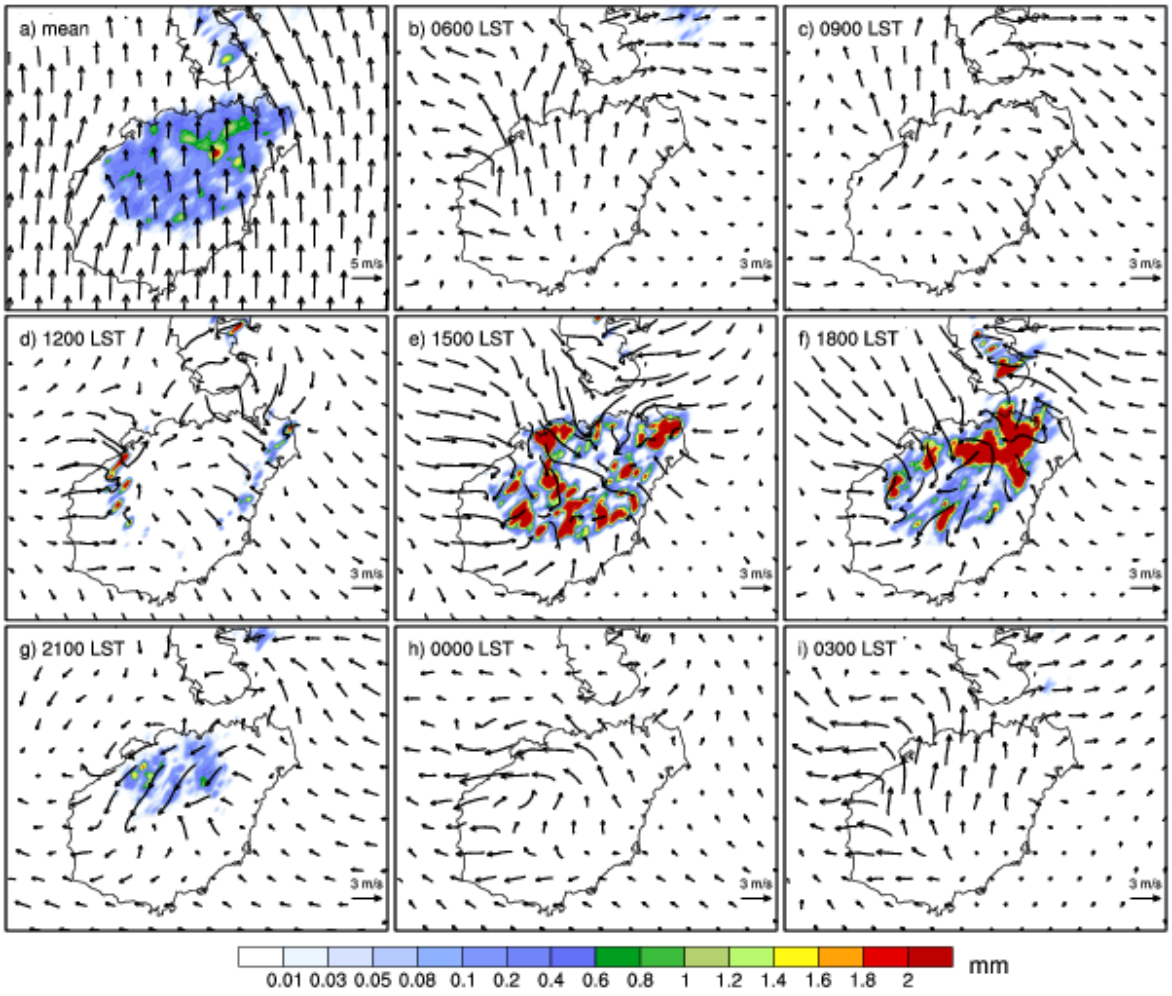

FIG. 9. As in FIG. 8, but for simulation NoTER.

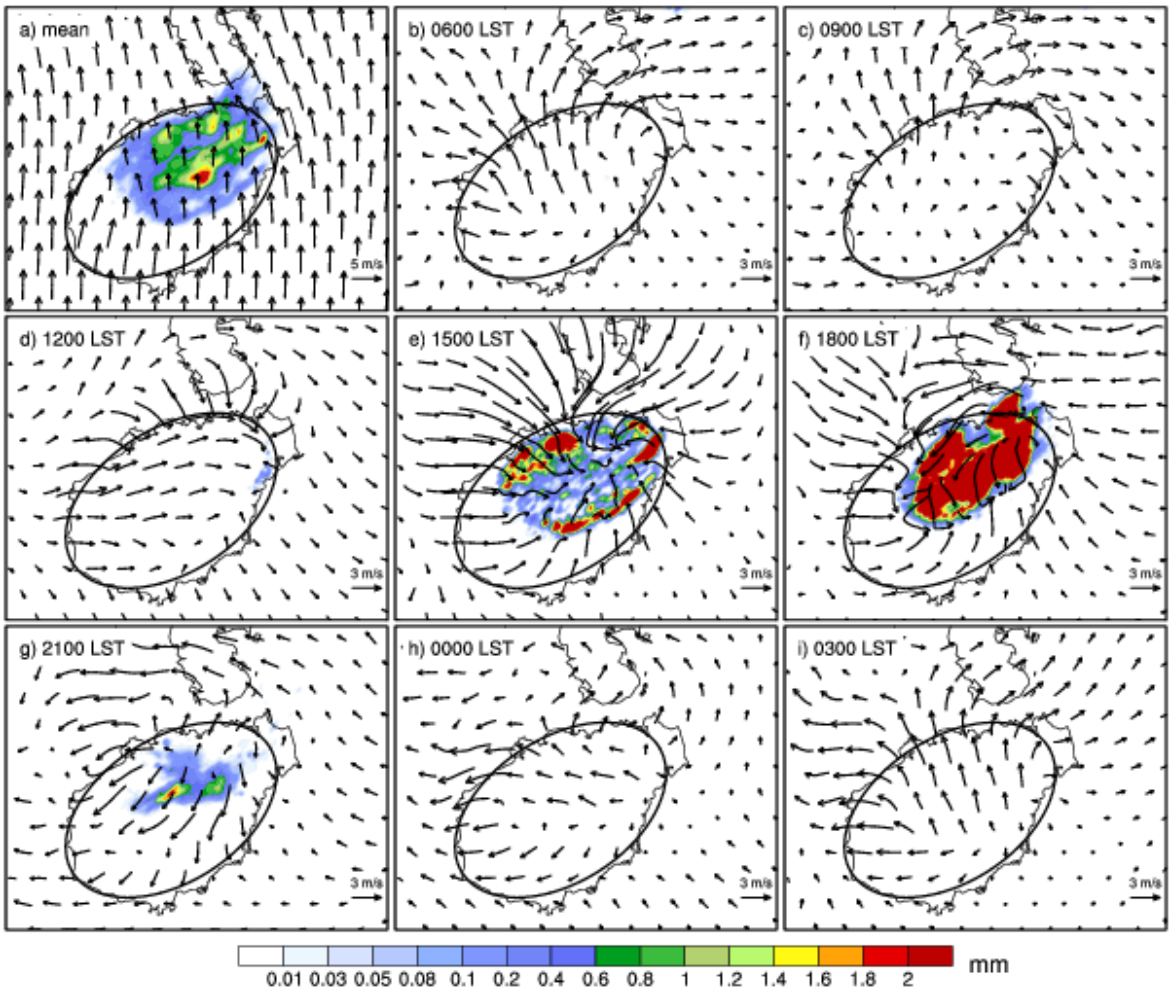

FIG. 10. As in FIG. 8, but for simulation IDEAL.

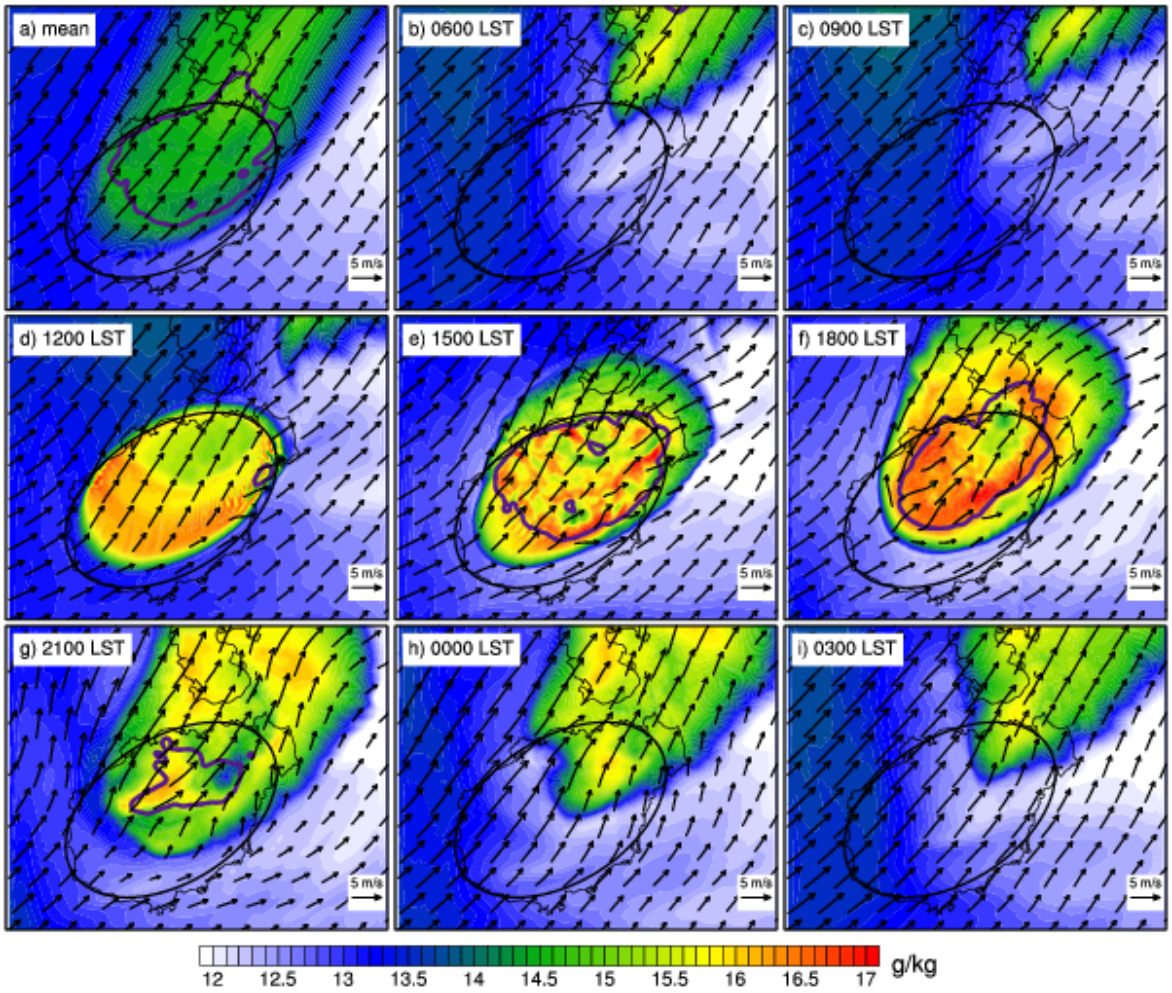

FIG. 11. Water vapor mixing ratio (shading) and horizontal wind (vectors) at 850 hPa, and hourly precipitation accumulations > 0.1 mm (thick purple contours), (b–i) every 3 h and (a) averaged over all times in IDEAL simulation.

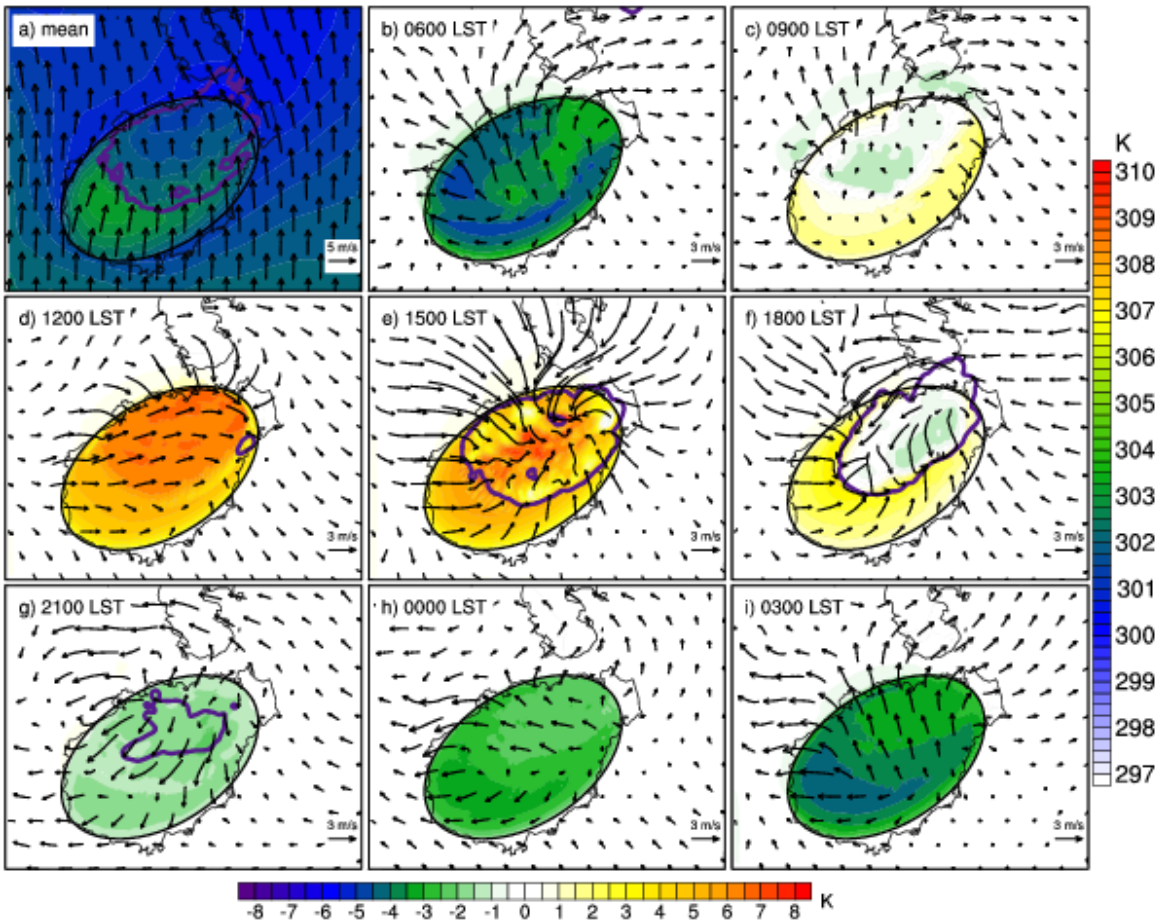

FIG. 12. (a) 2-meter mean temperature (shading) and horizontal wind (vectors) on the second lowest model level for horizontal wind; (b–i) 2-meter mean temperature perturbation (shading) and mean perturbation horizontal wind (vectors) on the second lowest model level every 3 h in IDEAL simulation. The right color bar is used for (a).

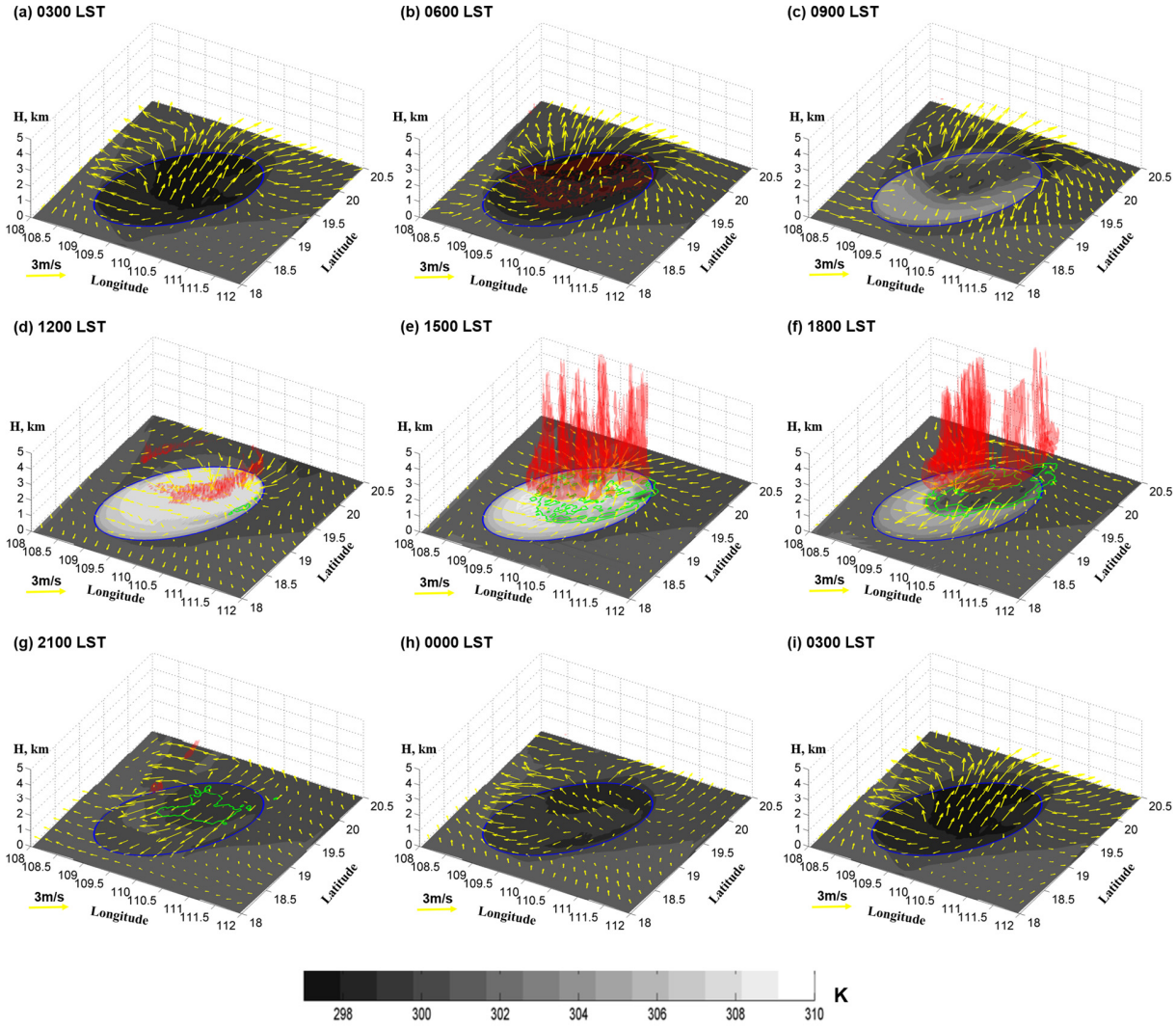

FIG. 13. Cloud water mixing ratio (red shading), 2-meter temperature (grey shaded), perturbation horizontal wind on the second lowest model level for horizontal wind (yellow vectors), and hourly precipitation accumulation (green contour lines) every 3 h in IDEAL simulation.

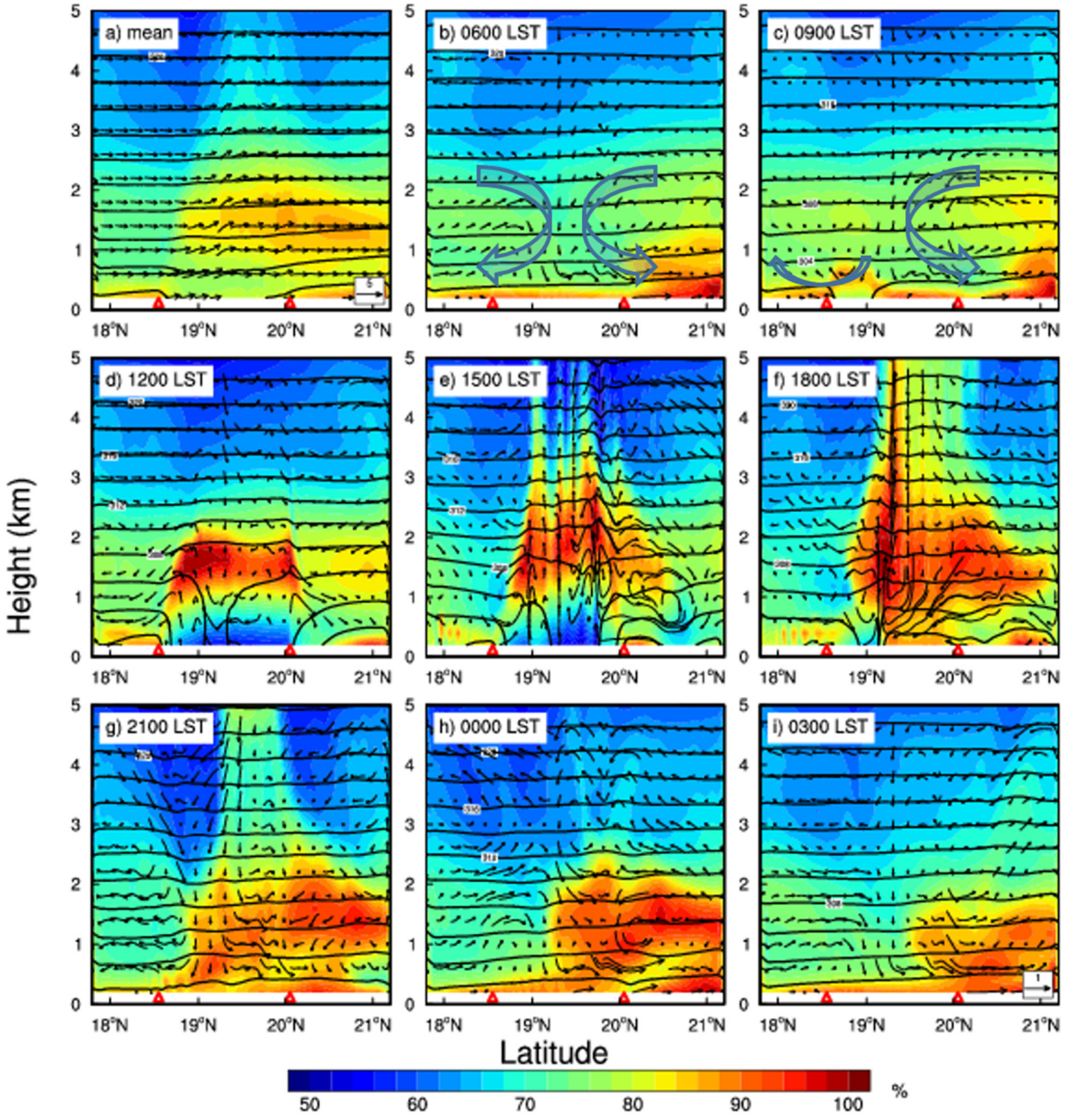

FIG. 14. Vertical cross-sections of relative humidity (shading), perturbation wind (vectors; the scale of the vertical component is increased by a factor of 5), and temperature (contours) in the south-to-north direction (see red line in Fig. 1) averaged over all hours (a) and at 3-h intervals (b–i) in IDEAL simulation. The triangles in each panel indicate the edges of the island. Arrows in b and c stand for the land breeze circulations.

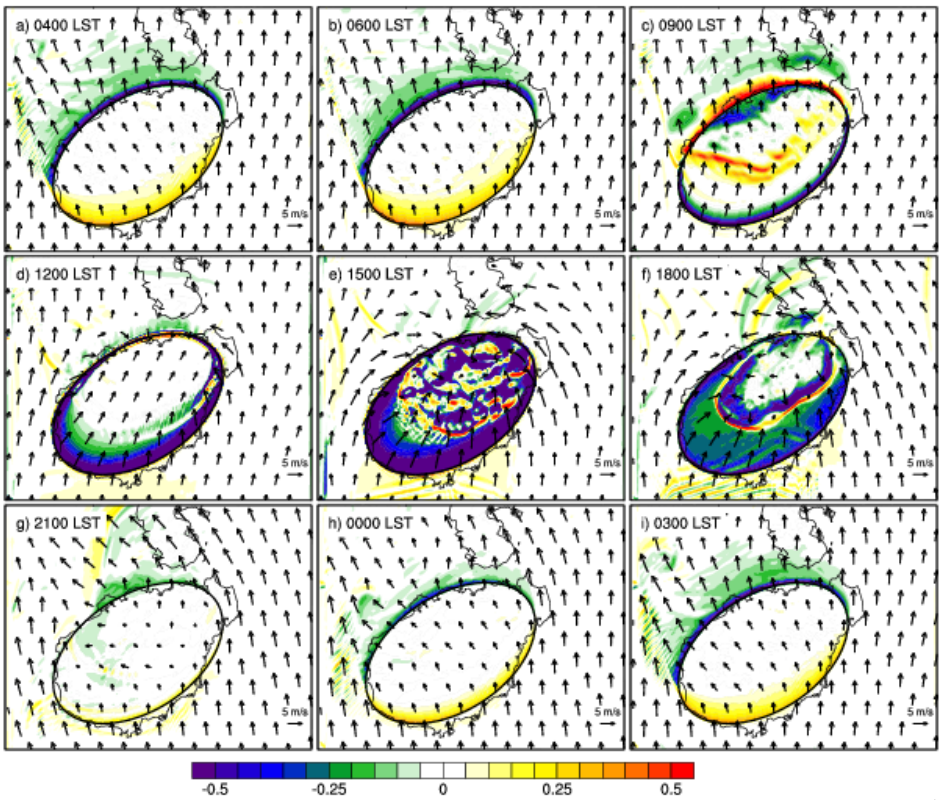

FIG. 15. Horizontal temperature advection (shaded) and horizontal wind (vector, m s^{-1}) on the first model level in simulation IDEAL.

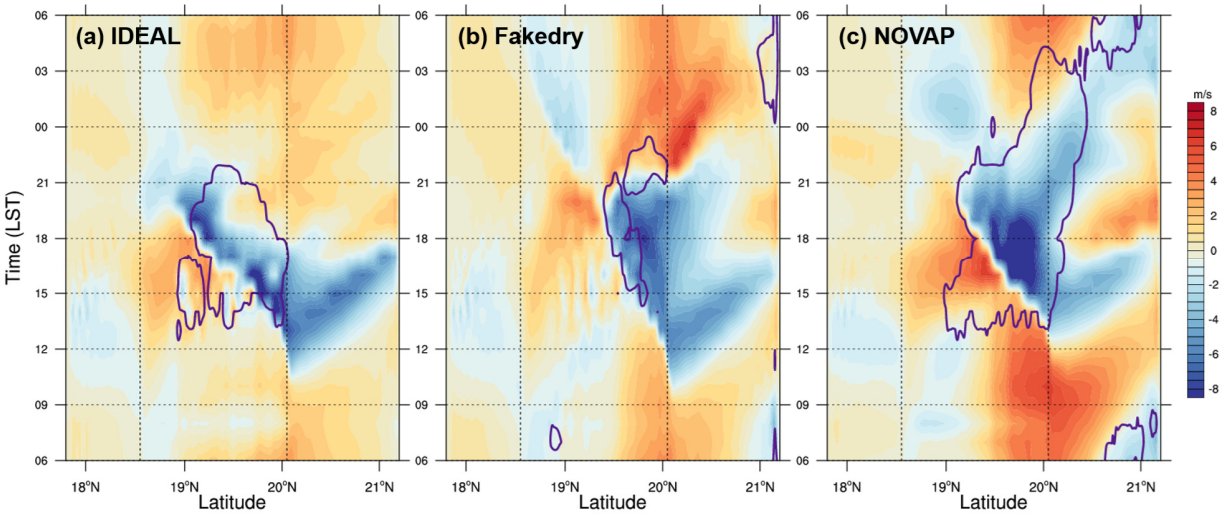

Fig. 16. Hovmoller diagrams of perturbation meridional wind component on the second lowest model level for horizontal wind (shading) in the (a) IDEAL, (b) Fakedry and (c) NOVAP simulations, respectively. Precipitation exceeding 0.1 mm h^{-1} is enclosed by the heavy purple contours. The two vertical dash lines indicate the edges of the island.